

# Microstructure and Mechanical Property of Al–Li Alloy Joint Formed by Electron Beam Welding with Filler Wire

Heng Jiang<sup>1</sup> · Shaogang Wang<sup>1</sup>  · Wen Zhang<sup>1</sup>

Received: 29 November 2023 / Accepted: 15 January 2024 / Published online: 21 February 2024  
© The Indian Institute of Metals - IIM 2024

**Abstract** The ER5183 is used as filler metal, and the Al–Li alloy is welded by electron beam welding. The microstructure and mechanical property of welded joint are investigated. Results show that, under the proper welding procedure, the joint with good appearance of weld is obtained. The fusion zone is mainly composed of  $\alpha$ -Al matrix phase and some strengthening phases involving  $\theta'$ (Al<sub>2</sub>Cu), T<sub>2</sub>(Al<sub>6</sub>CuLi<sub>3</sub>), T<sub>1</sub>(Al<sub>2</sub>CuLi) and  $\delta'$ (Al<sub>3</sub>Li). The grains in weldment are refined by the addition of electron beam scanning. Compared with that of the base metal (BM), the microhardness in weld zone is decreased to a certain extent. Under the welding condition of square wave electron beam scanning, the tensile strength of welded joint is 352.2 MPa, which is 70.2% of that of the BM. There exists obvious dimple morphology on the joint fracture surface, and it presents the characteristic of intergranular fracture.

**Keywords** Al–Li alloy · Electron beam welding with filler wire · Electron beam scanning · Microstructure · Mechanical property

## 1 Introduction

With the rapid development of aerospace industry, the weight reduction to aircraft component and improvement to structure performance were of great concern [1]. The existing results showed that, by the addition of a certain

content of element Li to aluminum alloy, the density of aluminum alloy could be reduced, while its elastic modulus was increased [2]. Al–Li alloys have excellent comprehensive properties such as low density, high specific strength and cryogenic performance. They are widely used in aerospace and other industrial fields [3, 4]. Because Al–Li alloys are often used to fabricate welded structure, the welding of Al–Li alloys is paid more attention. Electron beam welding (EBW) has the advantages of energy concentration, low heat input, narrow heat-affected zone (HAZ), large weld depth to width ratio and high welding efficiency, etc. It is suitable for the welding of Al–Li alloys.

Lin et al. [5] conducted the EBW of 5A90 Al–Li alloy. With the increase of electron beam current, the weld width was increased, and the grains in weldment were coarsened to a certain extent. Sahul et al. [6] investigated the microstructure and mechanical properties of 2099 Al–Li alloy EBW joint. During EBW process, the dissolution of strengthening phases resulted in the decrease of hardness in equiaxed grain zone (EQZ) of welded joint. Chen et al. [7] analyzed the mechanical properties of Al–Li alloy EBW joint. During welding, the evaporation loss of alloying elements with low boiling point led to less strengthening phases such as T<sub>1</sub>(Al<sub>2</sub>CuLi) and  $\theta'$ (Al<sub>2</sub>Cu) in weldment. It was the main reason for the decrease of joint mechanical property. The pressure was loaded to welding sample during EBW of 2195 Al–Li alloy, the evaporation loss of element Li was reduced in molten pool. The precipitation of strengthening phase T<sub>1</sub> was increased in weldment, thus the mechanical properties of welded joint were improved [8].

Compared with that of the autogenous EBW, some alloying elements can be supplemented to the weldment during EBW with filler wire. The morphology and distribution of low melting point eutectic are improved, thus the susceptibility to hot cracking is greatly reduced. Moreover, the weld

✉ Shaogang Wang  
sgwang@nuaa.edu.cn

<sup>1</sup> College of Materials Science and Technology, Nanjing University of Aeronautics and Astronautics, Nanjing 211106, China

formation can also be improved by the addition of filler metal. At present, there is few report on the EBW with filler wire for Al–Li alloys. In present work, the Al–Cu–Li alloy is welded by using EBW with filler wire. The effect of different welding procedures on microstructure and mechanical property of welded joint is investigated. Some guidance can be provided for the fabrication of Al–Li alloy welded structure in engineering application.

## 2 Materials and Procedure

The base metal (BM) is Al–Cu–Li alloy plate with the thickness of 2 mm, and its chemical composition is listed in Table 1. The main strengthening phase in the BM was  $T_1$ , as well as a small amount of precipitated phases involving  $\theta'$ ,  $\delta'(Al_3Li)$  and  $S(Al_2CuMg)$  [9]. The dimension of welding sample is 150 mm  $\times$  100 mm  $\times$  2 mm, and its type is butt joint. The welding wire ER5183 with the diameter of 1.2 mm is used, and its chemical composition is as follows (wt%): Al–5.08Mg–0.8Mn–0.03Cu–0.08Zn.

Before welding, the surface of welding sample is thoroughly cleaned. The welding equipment is EBOCAM EK150C-EG150-60BL type welding machine. During welding, the vacuum chamber pressure is  $8 \times 10^{-5}$  Pa, working distance 350 mm, accelerating voltage 120 kV, focusing current 2276 mA and wire feeding speed 27 mm/s. Moreover, in order to improve the weld formation and reduce the susceptibility to welding defects, electron beam scanning with different waveforms is introduced in the welding process. The scanning frequency is 150 Hz, and scanning amplitude is  $X = Y = 0.5$  mm. The welding parameters of EBW with filler wire are given in Table 2.

After welding, the Leica DMILM inverted optical microscope is used to observe the microstructure of welded joint. The electron back scatter diffraction (EBSD) is conducted to analyze the crystal orientation and grain size in weld cross-section. The experimental parameters are as follows: the test voltage is 20 kV, working distance 15 mm and scanning time 1.5 h. The mapping scanning analysis of alloying elements in weldment is carried out by using energy dispersive spectrometer (EDS). D8 Advance X-ray diffractometer (XRD) is used to identify the phase constituent of weld metal. The scanning range is  $10^\circ$ – $80^\circ$  and scanning rate  $2^\circ/\text{min}$ . The microstructure of fusion zone (FZ) is analyzed by using JEM-2100F transmission electron microscope (TEM). The acceleration voltage is 100 kV and beam diameter 2.0 nm. The microhardness in weld zone is measured by using

**Table 2** Welding parameters of joints by EBW with filler wire

| Sample no. | Electron beam current (mA) | Welding speed (mm/min) | Scanning waveform |
|------------|----------------------------|------------------------|-------------------|
| 1#         | 8                          | 700                    | Without scanning  |
| 2#         | 7                          | 700                    | Without scanning  |
| 3#         | 7                          | 900                    | Without scanning  |
| 4#         | 7                          | 700                    | Square wave       |
| 5#         | 7                          | 700                    | Circular wave     |
| 6#         | 7                          | 700                    | Triangular wave   |

HXS-1000A microhardness tester. Tensile test of welded joint is carried out by using KY-100KNW universal electronic material tester. Quanta 200 scanning electron microscope (SEM) is used to observe the tensile fracture morphology of joint, and the fracture characteristic is analyzed.

## 3 Results and Discussion

### 3.1 Weld Morphology

The macrographs of joint 2# and joint 4# are shown in Fig. 1. During welding, the fluidity of molten pool for joint 2# is relatively poor, and the weld morphology is influenced to a certain extent, as shown in Fig. 1a, b. In comparison, the weld formation of joint 4# is good, and it is fully penetrated. The top surface and root surface of welded joint are uniform, as shown in Fig. 1c, d. During EBW process, by the addition of appropriate filler wire, welding defects such as weld surface depression, undercut and microcrack can be avoided. In the welding of joint 4#, the electron beam scanning with square wave is introduced, and the good appearance of weld is obtained.

### 3.2 Microstructure of Welded Joint

Distance from weld surface about 1 mm, the microstructure of weld cross-section is analyzed. The microstructure of joint transition zone is shown Fig. 2. The welded joint is composed of HAZ, fine EQZ and FZ. The EQZ is near fusion line (FL), which is the typical microstructure in Al–Li alloy joint by fusion welding. Near EQZ, the microstructure of weldment is columnar crystal, which grows up perpendicular to the FL. They are formed by the pattern of epitaxial growth attached to the unmelted BM during solidification process.

**Table 1** Chemical composition of Al–Cu–Li alloy base metal (wt%)

| Cu      | Li      | Mg      | Mn      | Ag      | Zn       | Zr        | Al   |
|---------|---------|---------|---------|---------|----------|-----------|------|
| 3.4–4.2 | 0.6–0.9 | 0.6–1.1 | 0.1–0.5 | 0.1–0.5 | 0.3–0.45 | 0.04–0.18 | Bal. |

**Fig. 1** Macrograph of welded joint: **a** top surface of joint 2#, **b** root surface of joint 2#, **c** top surface of joint 4#, **d** root surface of joint 4#

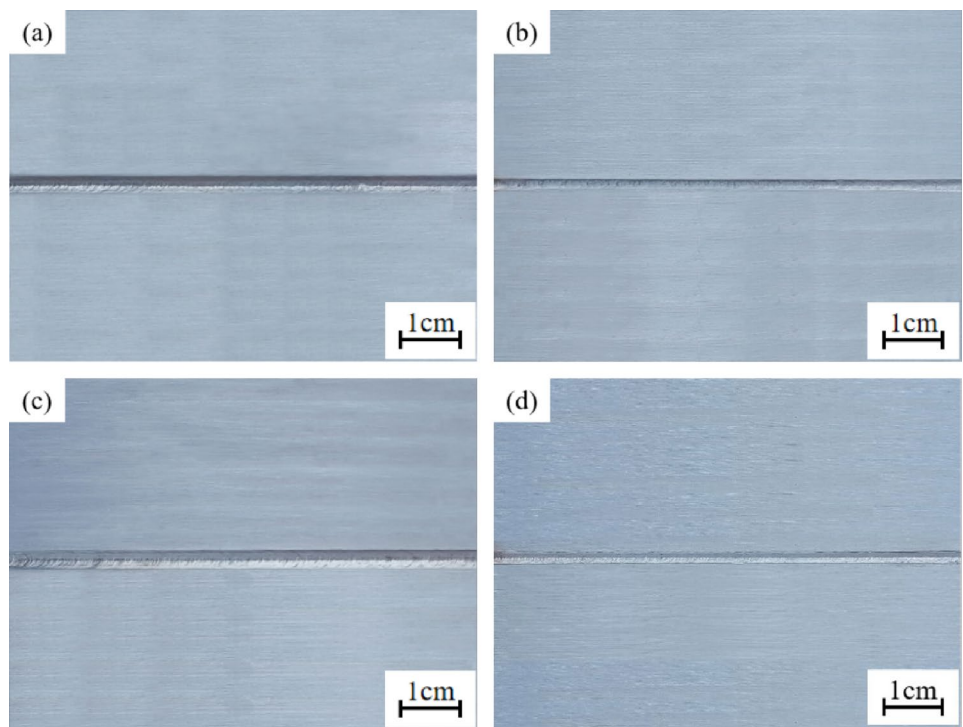
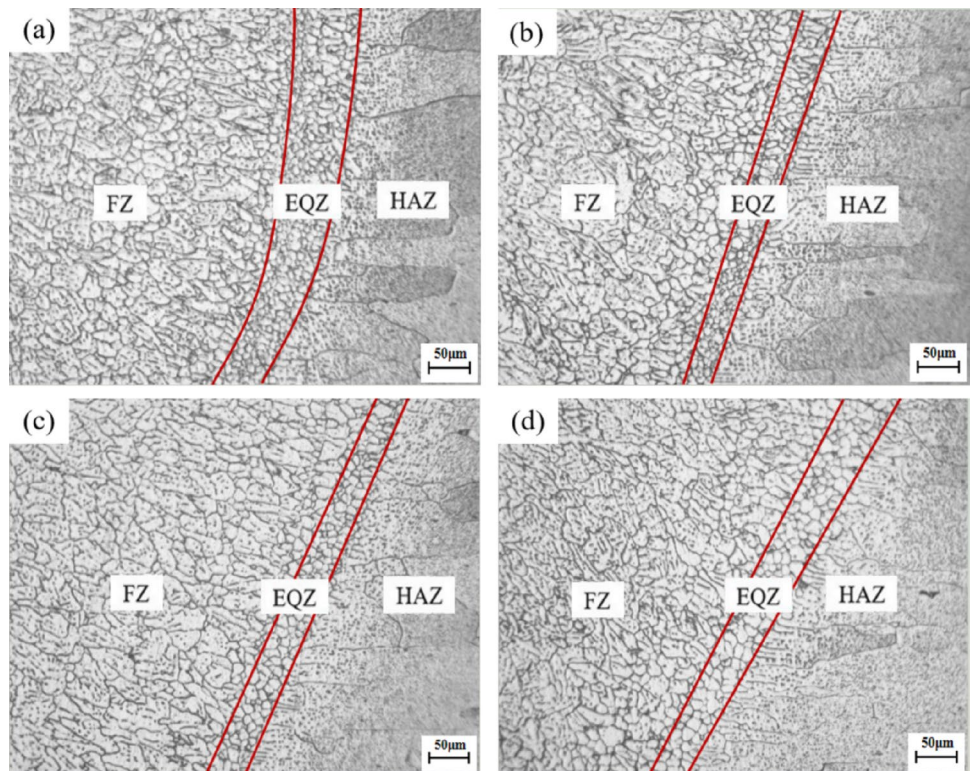


**Fig. 2** Microstructure of joint transition zone: **a** joint 2#, **b** joint 4#, **c** joint 5#, **d** joint 6#



Element Zr easily combines Al to form  $Al_3Zr$  compound with higher melting point, which results in the decrease of solid/liquid interfacial tension. The critical energy of heterogeneous nucleation is decreased. The temperature at fusion

boundary is slightly higher than the melting point of BM. There is a thin layer between the HAZ and columnar crystal, and more refractory particles  $Al_3Zr$  aggregate in this region. In addition, due to the surface activity of element Li, the

nucleation rate is increased, thus the fine equiaxed grains were formed [10, 11]. From EQZ to columnar crystal region, owing to the smaller supercooling degree and larger temperature gradient, the number of nucleus decreases. Attached to the EQZ, the columnar crystal nucleates and grows up with the epitaxial pattern. With the growth of columnar crystal, the temperature gradient is gradually decreased, which leads to the larger constitutional supercooling. Finally, the equiaxed dendrite is formed in weld center.

As shown in Fig. 2a, without electron beam scanning, the EQZ is relatively wide, and the columnar crystal region is larger. By the introduction of electron beam scanning during welding, the columnar crystals are broken up. Simultaneously, the stirring effect occurs to molten pool, and its fluidity is improved, which is advantageous to the heat and mass transfer of liquid metal. The strengthening phases in original BM are migrated and melted. As a result, the width of EQZ and columnar crystal region is decreased, as shown in Fig. 2b–d.

The microstructure of weld center is shown in Fig. 3. During welding, the cooling rate of molten pool is rapid, and the alloying elements near FL tend to aggregate in weld center. The constitutional supercooling is increased in weld center, and the growth of columnar crystal is inhibited. Subsequently, it is transformed into dendrite. With the square wave electron beam scanning, weld center is mainly composed of fine dendrite, as shown in Fig. 3b. Under the welding conditions of without scanning, circular and triangular

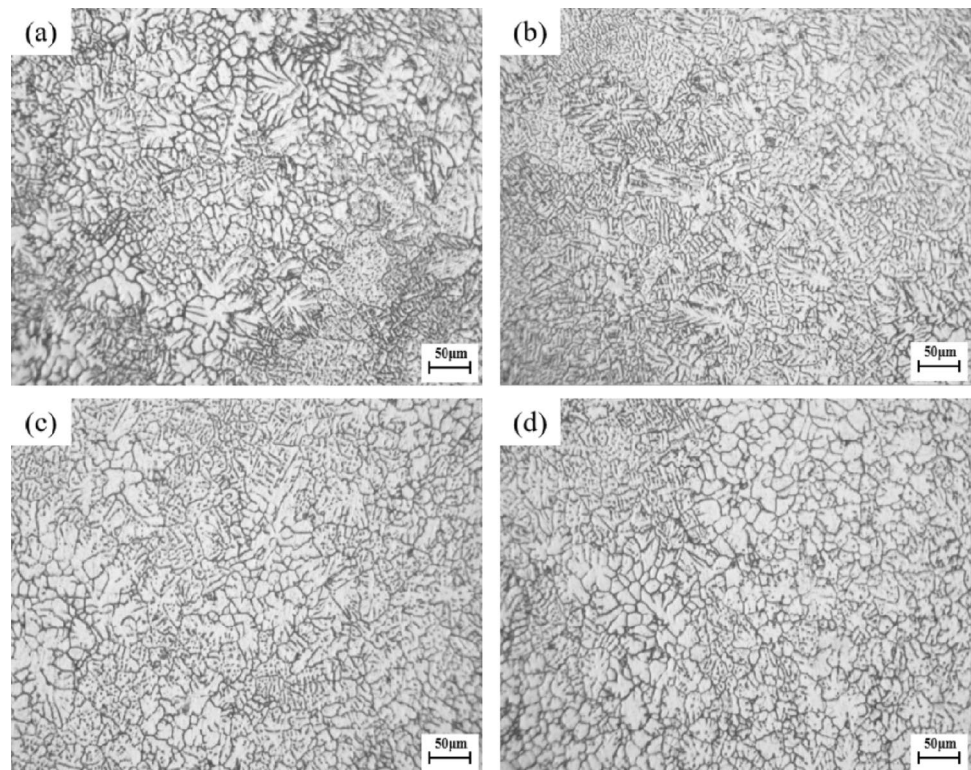
wave scanning, the dendrites in weld center are coarsened to a certain extent, as shown in Fig. 3a, c, d, respectively.

Figure 4 shows the crystallographic characteristics of grains in weld center under different welding conditions. Different colors represent different crystal orientations, namely grains with similar orientations having the same color. As shown in Fig. 4a, b, the proportion of several grains with different colors is basically the same, which means that the growth of grain has no obvious preferred orientation during solidification process. The texture is hardly found in weldment. Under the two welding conditions, the average grain size in weldment is 61.4  $\mu\text{m}$  and 50.1  $\mu\text{m}$ , respectively, as shown in Fig. 4c, d. Moreover, by the introduction of electron beam scanning during welding, the formed grains in molten pool break into fine dendrite arms, which can be acted as the heterogeneous nucleus. The quantity of nucleus increases. Consequently, the grains are refined under the welding condition of square wave electron beam scanning.

### 3.3 Distribution of Alloying Elements and Phase Constituent

SEM image of joint 2# is shown in Fig. 5a. It is mainly composed of eutectic structure, and some secondary phases precipitate at grain boundary. The mapping scanning analysis of alloying elements is carried out, and the distribution images of elements Cu and Mg are shown in Fig. 5b, c,

**Fig. 3** Microstructure of weldment: **a** joint 2#, **b** joint 4#, **c** joint 5#, **d** joint 6#



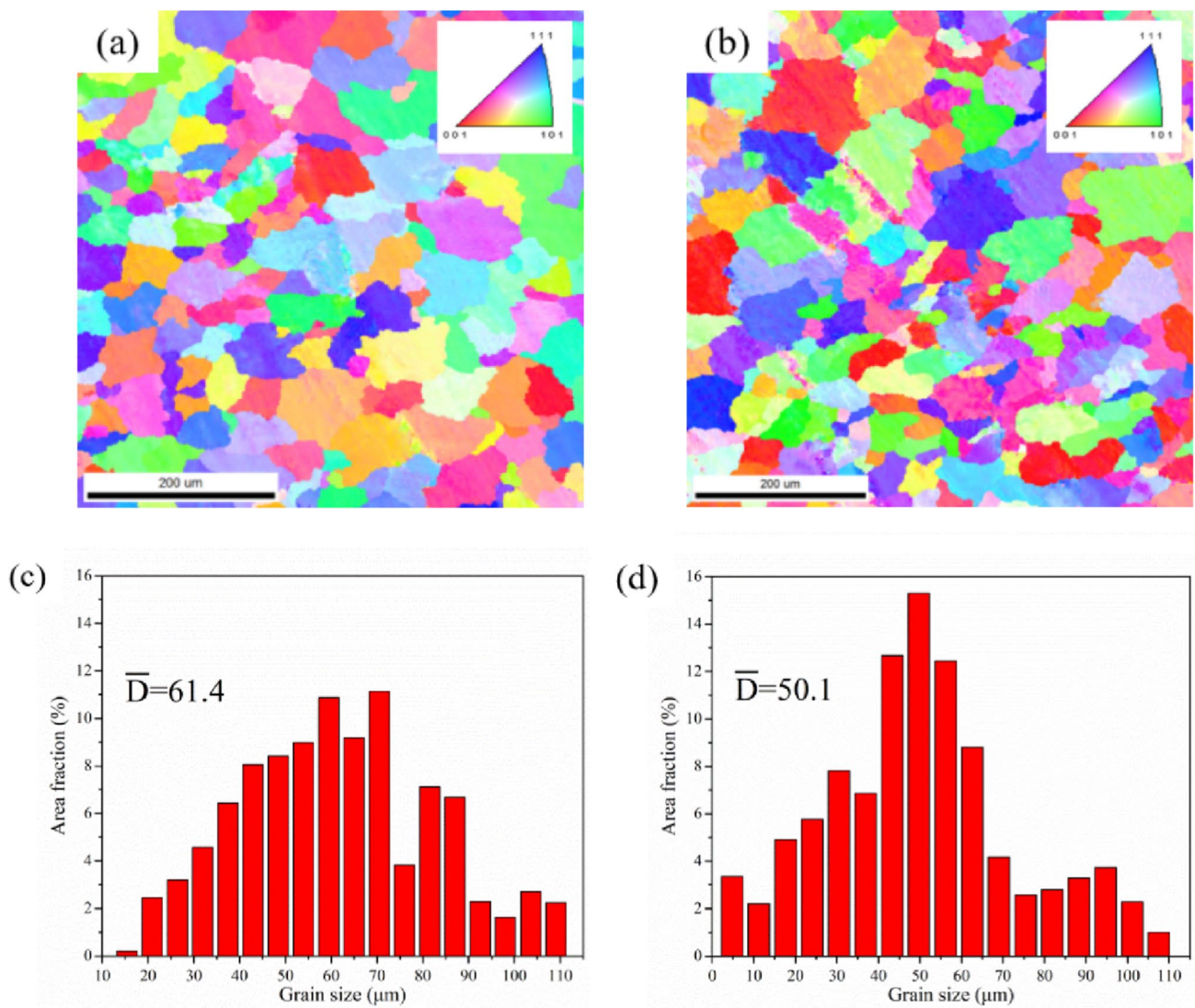


**Fig. 4** EBSD image of weldment: **a** inverse pole figure of joint 2#, **b** inverse pole figure of joint 4#, **c** grain size of joint 2#, **d** grain size of joint 4#

respectively. At grain boundary, the distribution of Cu element is brighter. It means that the content of Cu element is obviously increased at grain boundary, while it is decreased within grains. During the cooling process, the solute atoms in liquid metal are partially mixed through convection and diffusion. In that case, the concentration of solute element in solid phase could be described by the following equation [12]:

$$C_s = K_{eq} C_0 (1 - f_s)^{K_{eq} - 1} \tag{1}$$

where  $C_s$  is the concentration of solute,  $K_{eq}$  is the equilibrium partition coefficient of solute,  $C_0$  is the initial concentration of solute, and  $f_s$  is the volume percentage of solid phase. The distribution of alloying elements mainly depends on the value of  $K_{eq}$ . When the value is lower than

one ( $K_{eq} < 1$ ), some solutes will be excluded from the liquid phase at interface. In the continuous solidification process, the concentration of solute element will be gradually increased. Because the  $K_{eq}$  of Cu element is lower than one, some Cu elements segregate at grain boundary after solidification.

Due to the segregation of Cu element in molten pool, the degree of supersaturation will be insufficient in  $\alpha(Al)$  solid solution. The precipitation of strengthening phase is fewer in as-welded (AW) condition. By the introduction of electron beam scanning during welding, the fluidity of molten pool is enhanced, which promotes the redistribution of Cu element in weldment. The segregation of alloying elements is reduced at grain boundary, as shown in Fig. 5e.

As shown in Fig. 5c, f, the distribution of Mg element is relatively uniform in weldment. During welding, it is

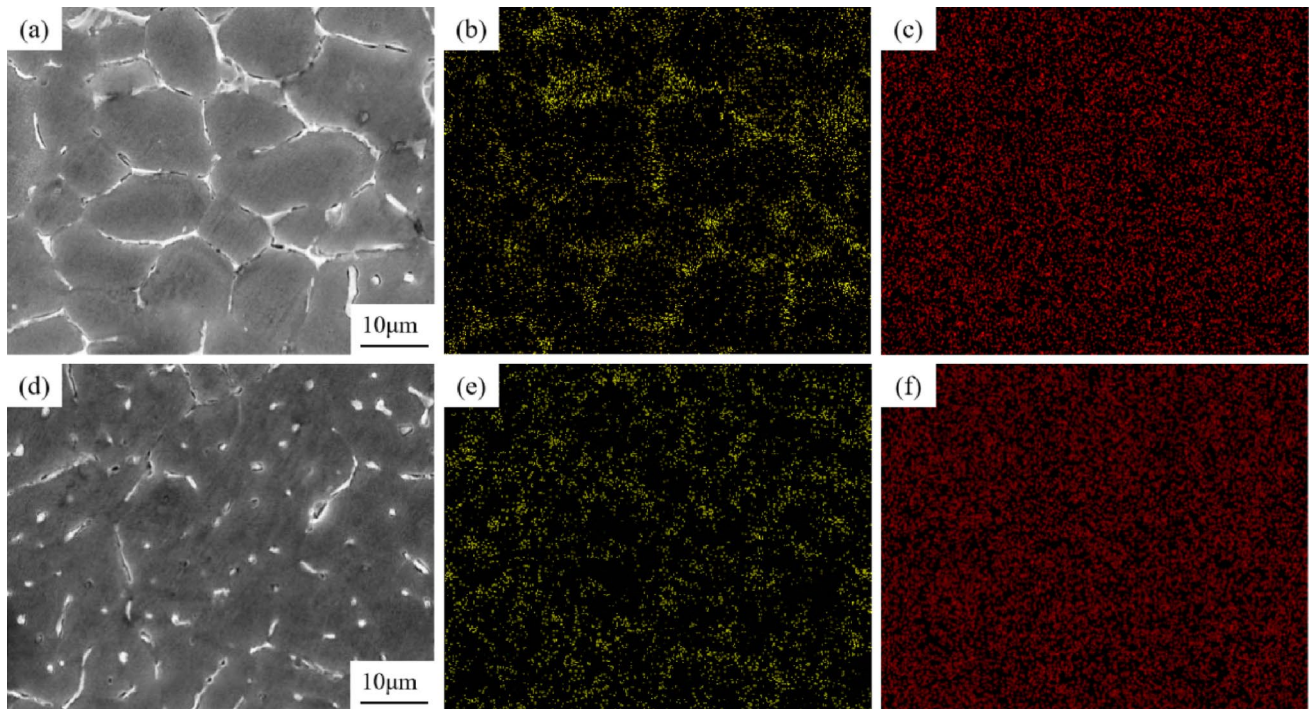


**Fig. 5** SEM image of weldment and distribution of alloying elements: **a** joint 2#, **b** Cu distribution in (a), **c** Mg distribution in (a), **d** joint 4#, **e** Cu distribution in (d), **f** Mg distribution in (d)

mainly dissolved in the Al matrix. In the fusion welding process of Al–Li alloys, the low melting point eutectic easily aggregates at grain boundary to form liquid film. Under the action of shrinkage stress, the liquid film fractured to form solidification cracks [13, 14]. In present work, by the addition of filler wire and electron beam scanning, the quantity of eutectic structure is increased, and the fluidity of molten pool is improved. Consequently, the hot cracking is effectively avoided.

Figure 6 shows the XRD analysis of weld metal. There are mainly diffraction peak of  $\alpha$ (Al), and some diffraction peaks of strengthening phases such as  $T_1$ ,  $\theta'$ ,  $T_2$ ( $Al_6CuLi_3$ ) and  $\delta'$ . During welding, by the addition of Al–Mg welding wire, the chemical composition of weld metal is changed. As a result, the precipitation of strengthening phases is also varied in weldment. According to Reference [15], the structure of icosahedra in Al–Cu–Mg and Al–Cu–Li alloys is similar. In the Al–Cu–(Li, Mg) alloy, Li atoms can be replaced by Mg atoms to form the quasicrystalline phase  $Al_6Cu(Li, Mg)_3$ , and it is also considered as the  $T_2$  phase. In the molten pool with high content of Mg element, its chemical composition satisfies the nucleation of  $T_2$  phase, thus it easily precipitates in weldment.

Because the size of Mg atom is larger, the addition of Mg element will change the lattice constant, but it has no great effect on the phase constituent. Figure 6 shows that no Mg-containing phase is found. The increase of Mg element will

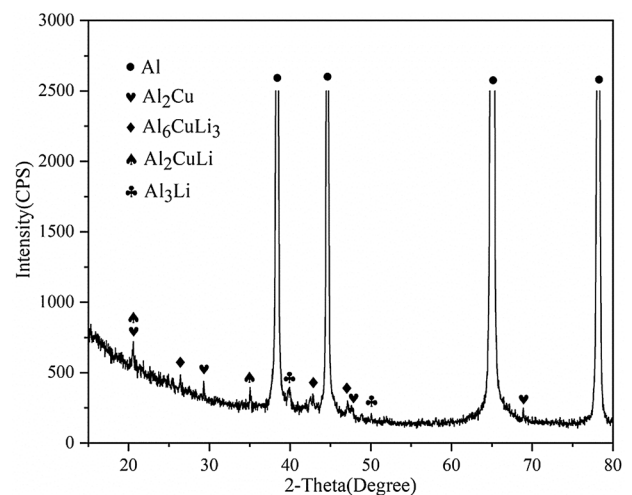
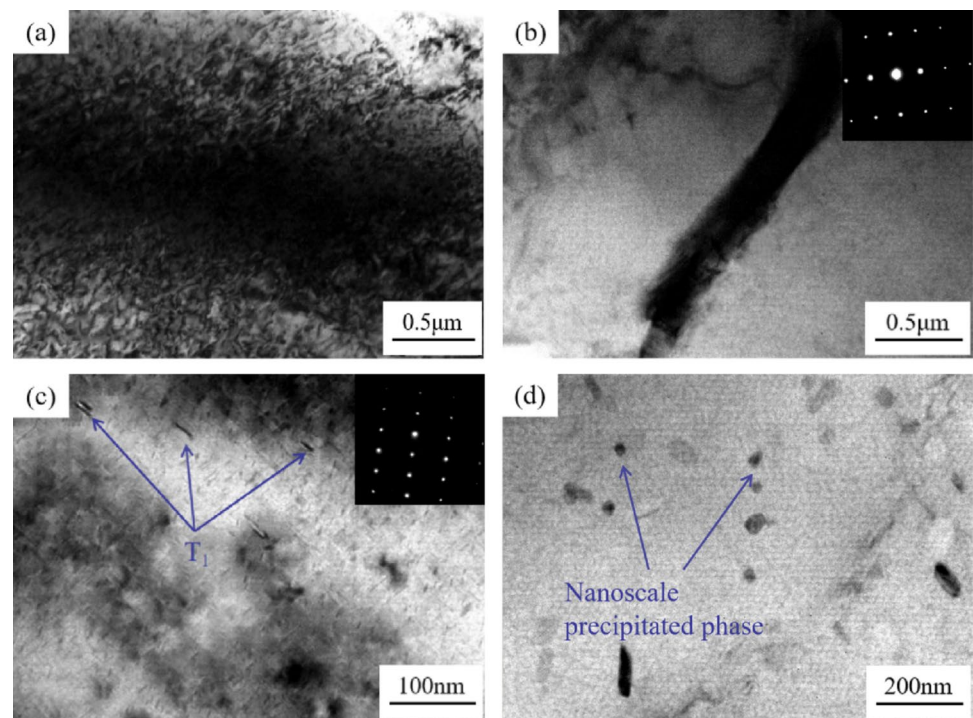


**Fig. 6** XRD pattern of weldment

change the solubility of elements Cu and Li in the Al matrix. The segregation of elements Cu and Li at grain boundary promotes the formation of  $T_2$  phase. The distribution of  $T_2$  phase is dispersed in weldment, which was beneficial to reduce the tendency to intergranular fracture [16, 17].

Figure 7 shows the TEM images of FZ. As shown in Fig. 7a, there are a lot of dislocations in weldment. They are entangled with each other, and the weldment is strengthened

**Fig. 7** TEM image of FZ: **a** dislocations in weldment, **b**  $\theta'$ (Al<sub>2</sub>Cu) phase, **c** T<sub>1</sub>(Al<sub>2</sub>CuLi) phase, **d** nanoscale precipitated phase



to a certain extent. The rod-like strengthening phase in Fig. 7b is the  $\theta'$  phase. The needle-like strengthening phase in Fig. 7c is the T<sub>1</sub> phase. T<sub>1</sub> phase presents the hexagonal structure, and it has the semi-coherent relationship to the matrix habit plane of  $\{111\}_{Al}$  [18, 19]. The gliding plane in Al–Li alloy is  $\{111\}$ , and the T<sub>1</sub> phase can effectively inhibit the movement of dislocations. There are precipitated phases within grains, as shown in Fig. 7d. They are relatively fine and present near-spherical. They non-uniformly distribute in the  $\alpha$ (Al) matrix, and these intragranular precipitated phases were  $\delta'$  phase [20]. The  $\delta'$  phase is a metastable phase, and it has coherent relationship to the Al matrix. It has the L1<sub>2</sub>-type ordered superlattice structure, and its lattice constant is similar to that of the Al matrix, with small degree of mismatch [21, 22]. Because the interfacial energy of  $\delta'$  phase is low, the driving force to nucleation is small. The critical size of nucleus is smaller, thus the precipitation of  $\delta'$  phase is relatively easy.

In the process of EBW with filler wire, the cooling rate of molten pool is rapid, and the diffusion of atoms is insufficient. There is not enough time for the precipitation of T<sub>1</sub> phase from solid solution. Consequently, the quantity of T<sub>1</sub> phase in weldment is less. The precipitation of nanoscale spherical  $\delta'$  phase is dominant in weldment.

### 3.4 Microhardness Distribution

The distribution of microhardness in weld zone with different welding procedures is shown in Fig. 8. The hardness

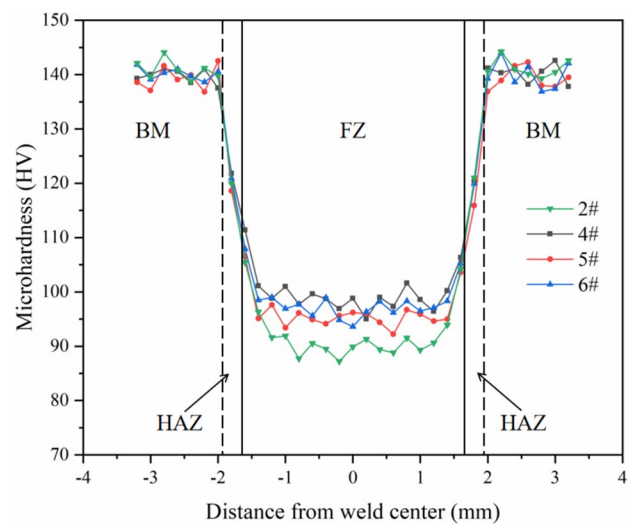


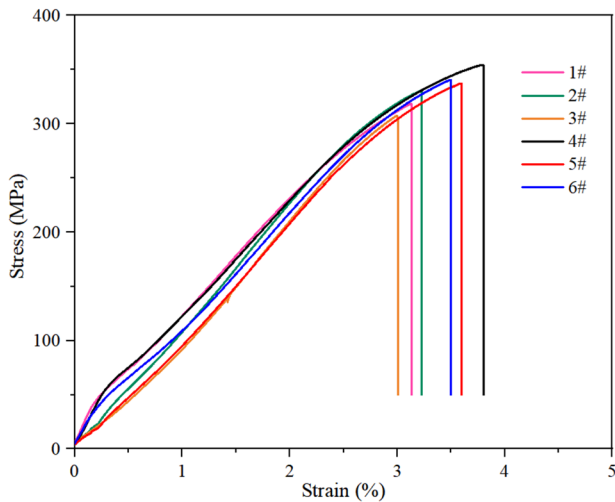
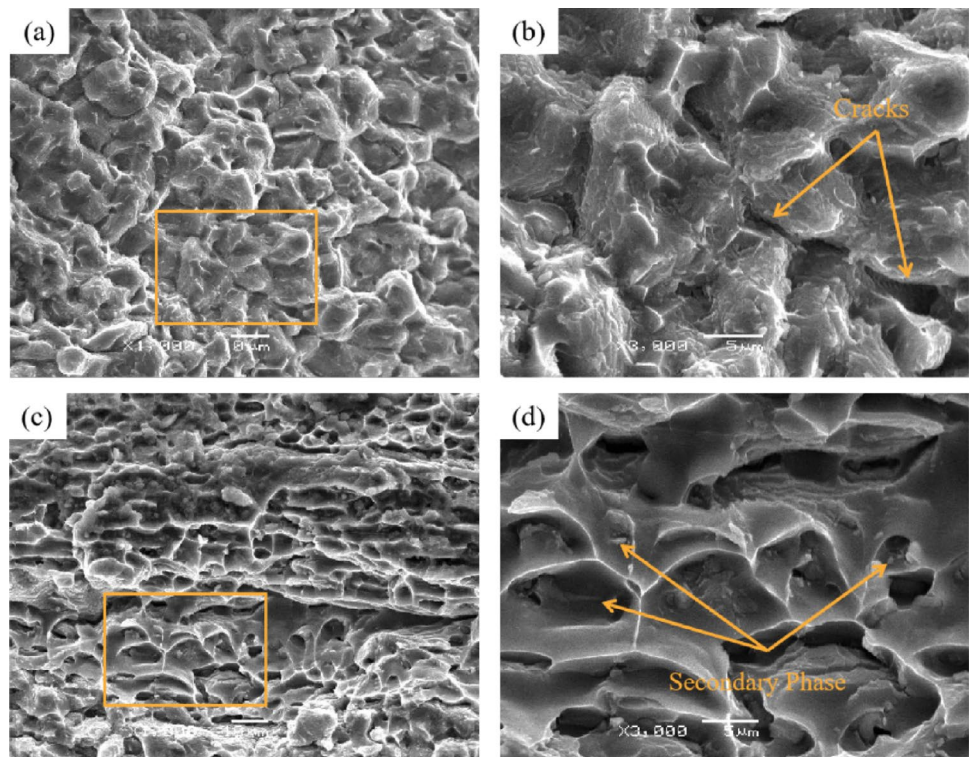
**Fig. 8** Microhardness distribution of joints with different scanning modes

distribution is symmetrical to the weld centerline. The value of hardness is ranked as follows: BM > HAZ > FZ, and the hardness in FZ is obviously decreased. Softening phenomenon occurs to weld zone in AW condition.

The temperature of molten pool is high during welding, and some alloying elements are evaporated and lost. In addition, the alloying elements segregate at grain boundary, which causes the decrease of alloying elements within grains. The supersaturation degree of Al matrix is

**Table 3** Results of tensile tests of welded joints

| Sample no. | Ultimate tensile strength (MPa) | Yield strength (MPa) | Elongation (%) |
|------------|---------------------------------|----------------------|----------------|
| 1#         | 319.2 ± 1.4                     | 226.6 ± 1.1          | 3.1 ± 0.1      |
| 2#         | 324.8 ± 1.2                     | 229.2 ± 1.4          | 3.2 ± 0.2      |
| 3#         | 303.6 ± 3.0                     | 207.5 ± 2.1          | 3.0 ± 0.1      |
| 4#         | 352.2 ± 2.6                     | 256.5 ± 2.4          | 3.8 ± 0.3      |
| 5#         | 333.3 ± 2.2                     | 239.3 ± 1.6          | 3.6 ± 0.3      |
| 6#         | 338.7 ± 2.8                     | 243.1 ± 2.3          | 3.5 ± 0.2      |

**Fig. 9** Stress–strain curves of welded joints**Fig. 10** SEM images of joint tensile fracture: **a** joint 2#, **b** magnification of yellow rectangle in **a**, **c** joint 4#, **d** magnification of yellow rectangle in **c**

insufficient, and the quantity of strengthening phases precipitated in weldment is less. Consequently, the hardness in FZ decreases.

Figure 8 shows that the hardness in FZ of joint 4# with square wave scanning is higher than those of the other, because the grains in weldment is relatively fine, as shown in Figs. 3 and 4. Grain refinement is beneficial to the increase of hardness in weld zone.

### 3.5 Tensile Property and Fracture Analysis

The tensile strength of BM is 501.5 MPa, and its elongation is 13.9%. The results of tensile tests for welded joints under different welding procedures are listed in Table 3. The corresponding stress–strain curves are shown in Fig. 9. During stretching, the joint fracture occurs to weld metal. The tensile strength of joint 4# is the maximum. It reaches to 352.2 MPa, which is 70.2% of that of the BM.

Compared with the similar results of Al–Li alloy laser beam welding joint [20, 23], the tensile strength of joint 4# is obviously improved. During welding, the alloying elements in weldment are supplemented by the addition of welding wire. Under the action of electron beam scanning, the alloying elements uniformly distribute in weldment, and the solution strengthening effect is enhanced. The degree of supersaturation of  $\alpha(\text{Al})$  solid solution is increased, and the quantity of secondary phase is increased, thus the precipitation strengthening effect is improved. Moreover, the grain in weldment is refined by



the introduction of electron beam scanning, which leads to the obvious grain refinement strengthening effect. Consequently, the mechanical property of welded joint is greatly improved.

Figure 10 shows the tensile fracture morphology of welded joint. The fracture image of joint 2# is shown in Fig. 10a. There are some dimples on the fracture surface, but the dimples are relatively small and shallow. Moreover, there are microcracks on the fracture surface, as shown in Fig. 10b. It is characterized by the pattern of intergranular fracture. The fracture morphology of joint 4# is shown in Fig. 10c. There are obvious tearing edges on the fracture surface. As shown in Fig. 10d, many dimples distribute on the fracture surface, and there are some secondary phase particles at the bottom of dimples. It still has a certain tendency to intergranular fracture during stretching, as shown in Fig. 10c.

#### 4 Conclusions

- (1) Under the appropriate welding procedure, the joint with good appearance of weld is obtained. The FZ is mainly composed of  $\alpha$ -Al matrix phase and some strengthening phases involving  $\theta'$ ,  $T_2$ ,  $T_1$  and  $\delta'$ .
- (2) By the addition of welding wire and electron beam scanning, the alloying elements are supplemented and they uniformly distribute in weldment. The combined effect involving precipitation strengthening, grain refinement strengthening and solution strengthening contributes to the mechanical performance of welded joint.
- (3) The microhardness in FZ is decreased to a certain extent. By the introduction of square wave electron beam scanning, the tensile strength of welded joint is the maximum, and its strength coefficient reaches to 70.2%. There exists obvious dimple morphology on the fracture surface, and it is characterized by the pattern of intergranular fracture.

**Acknowledgements** This project is supported by the Key Research and Development Program of Zhenjiang City (No. GY2019004), which is gratefully acknowledged.

#### References

1. Zhang X Y, Huang T, Yang W X, Xiao R S, Liu Z, Li L, *J Mater Process Technol* **237** (2016) 301.
2. Sun Z Y, He B, Li K J, Tu Y X, Wang H M, *J Alloys Compd* **908** (2022) 164630.
3. Duan S W, Wang T, Zou Y, *Trans Indian Inst Met* **72** (2019) 1733.
4. Dursun T, Soutis C, *Mater Des* **56** (2014) 862.
5. Lin B, Chen L, Cheng D H, *Adv Mater Res* **1095** (2015) 906.
6. Sahul M, Sahul M, Haršáni M, Dománková M, *Mater Lett* **276** (2020) 128276.
7. Chen G Q, Yin Q X, Zhang G, Zhang B G, *J Manuf Process* **50** (2020) 216.
8. Chen G Q, Yin Q X, Zhang G, Zhang B G, *Mater Des* **188** (2020) 108439.
9. Liu F C, Zhou B S, Mao Y Q, Huang C P, Chen Y H, Wang Z T, *Mater Sci Technol* **34** (2018) 111.
10. Chen L, Hu Y N, He E G, Wu S C, Fu Y N, *Int J Light Mater Manuf*, **1** (2018) 169.
11. Shao Y K, Li X Y, Chen L, He E G, *Metall Mater Trans B* **52** (2021) 1413.
12. Ferreira A F, Ferreira I L, Almeida R P, Castro J A, Sales R C, Junior Z A, *Trans Nonferrous Met Soc China* **31** (2021) 1853.
13. Xiao R S, Zhang X Y, *J Manuf Process* **16** (2014) 166.
14. Agilan M, Phanikumar G, Sivakumar D, *Trans Indian Inst Met* **71** (2018) 2667.
15. Shen Y, Shifflet G J, Poon S J, *Phys Rev B* **38** (1998) 5332.
16. Yin Q X, Chen G Q, Teng X Y, Huang X Y, *Mater Sci Eng A* **851** (2022) 143662.
17. Zhang X J, Wang H W, Yan B, Zou C M, Wei Z J, *J Alloys Compd* **867** (2021) 159096.
18. Shao Y K, Li X Y, Chen L, He E G, *J Alloys Compd* **895** (2022) 162717.
19. Ning H, Li J F, Ma P C, Chen Y L, Zhang X H, Zhang K, Zhang R F, *Vacuum* **182** (2020) 109677.
20. Zhang X Y, Yang W X, Xiao R S, *Mater Des*, **88** (2015) 446.
21. Zhang X L, Zhang L, Wu G H, Shi C C, Zhang J S, *J Mater Sci* **54** (2019) 791.
22. Pletcher B A, Wang K G, Glicksman M E, *Acta Mater* **60** (2012) 5803.
23. Ning J, Zhang L J, Bai Q L, Yin X Q, Niu J, Zhang J X, *Mater Des* **120** (2017) 144.

**Publisher's Note** Springer Nature remains neutral with regard to jurisdictional claims in published maps and institutional affiliations.

Springer Nature or its licensor (e.g. a society or other partner) holds exclusive rights to this article under a publishing agreement with the author(s) or other rightsholder(s); author self-archiving of the accepted manuscript version of this article is solely governed by the terms of such publishing agreement and applicable law.